Results in Engineering 25 (2025) 103581

Contents lists available at ScienceDirect

Results in Engineering

journal homepage: www.sciencedirect.com/journal/results-in-engineering

Continuous-flow mechanochemical preparation of Ag-Cu@ZIF-8 bimetallic system for antimicrobial applications

Ana I. Martín-Perales [a,b], Manuel Peña-Ortiz [a,c], Juliana Alves Resende [d], Irene Malpartida [b], Rafael Luque [e,f], Alina M. Balu [a,*]

[a] Departamento de Química Orgánica, Facultad de Ciencias, Campus de Rabanales, Universidad de Córdoba, Ctra Nnal IV-A km 396, 14014, Córdoba, Spain
[b] Deasyl S.A., Chemin du Pont-du-Centenaire, Genève, Switzerland
[c] Departamento de Ingeniería Química y Química Inorgánica, Facultad de Ciencias, Campus de Rabanales, Universidad de Córdoba, Ctra Nnal IV-A km 396, 14014, Córdoba, Spain
[d] Universidade Federal do Espírito Santo - UFES, Departamento de Farmácia e Nutrição, 29500-000, Alegre, ES, Brasil
[e] Peoples Friendship University of Russia (RUDN University), 6 Miklukho Maklaya Str., 117198, Moscow, Russian Federation
[f] Universidad ECOTEC, Km. 13.5 Samborondón, Samborondón, EC092302, Ecuador

ARTICLE INFO

Keywords:
Metal-organic frameworks
Antibacterial
Antifungal
Bimetallic systems
ZIF-8
Flow mechanochemistry

ABSTRACT

This study discloses the synthesis of Ag- and Cu- modified ZIF-8 materials using a novel, sustainable beads-assisted flow reaction in a continuous-flow mechanochemical system. This approach offers an efficient, environmentally friendly route to producing antimicrobial materials with promising applications. Antimicrobial tests against *Escherichia coli, Staphylococcus aureus*, and *Candida albicans* revealed that pristine ZIF-8 showed no relevant biological activity. Ag@ZIF-8 comparably demonstrated strong bactericidal activity against *E. coli* and *S. coli* at 0.1 mg mL^{-1}, while Cu@ZIF-8 exhibited moderate antibacterial activity against *S. aureus* (0.5 mg mL^{-1}, 5 % Cu loading) and no activity against *E. coli* or *C. albicans*. Notably, bimetallic Ag-Cu@ZIF-8 composite (5 % Ag + 5 % Cu) displayed enhanced antibacterial efficacy including antifungal activity against *C. albicans* at a concentration of 0.1 mg mL^{-1}, likely due to a synergistic effect between Ag and Cu ions.

1. Introduction

Metal-organic frameworks (MOFs) are highly appealing materials, owing to their remarkable properties which encompass large surface areas, substantial pore volumes and tunable pore sizes [1,2]. These characteristics make MOFs versatile and valuable in various applications, including gas storage [3,4], catalysis [5,6], drug delivery [7,8], and sensing [9,10]. The modular nature of MOFs, derived from the combination of metal nodes and organic linkers, enables a wide range of design possibilities, allowing researchers to tailor their properties for specific purposes [11]. This adaptability, coupled with their intriguing structural features, positions MOFs as promising candidates for addressing diverse challenges in materials science and related fields.

To date, over 90,000 MOFs have been reported, with over 500,000 MOF structures predicted, providing a seemingly unlimited number of MOF structures for study and application [12]. In recent years, zeolitic imidazolate frameworks (ZIFs) have rapidly developed, representing a sub-family of MOFs and having a similar topology to that of zeolites [13]. ZIFs combine the advantages of both MOFs and zeolites since they have properties of these two materials, such as crystallinity, porosity, and enthralling chemical and thermal stability [14,15]. Comprising transition metals such as Zn, Cu, Co, and Fe, they are structured with tetrahedral coordination to an imidazolate-based linker, such as 2-methyl imidazole (HmIm). In the case of ZIF-8, this framework features a Zn node coordinated to Hmim through its two nitrogen atoms and its chemical formula is $Zn(mim)_2$ [16].

Notably, the angle between the metal-linker-metal (M-IM-M) components closely mirrors the angle observed in zeolites, approximately 145°. This resemblance led to the designation of zeolitic imidazolate frameworks, indicating a zeolite-like topology. Specifically, ZIF-8 adopts the topology of sodalite (SOD). The unique structural features of ZIF-8 contribute to the special properties and potential applications of ZIF-8 and other ZIF materials [17–19].

The antimicrobial applications of ZIF-8 and ZIF-8-based composites hold significant promise (Table 1), primarily attributed to their highly porous structure and the capacity to serve as reservoirs for metal ions,

---

* Corresponding author.
E-mail address: qo2balua@uco.es (A.M. Balu).

https://doi.org/10.1016/j.rineng.2024.103581
Received 20 September 2024; Received in revised form 22 November 2024; Accepted 28 November 2024

Table 1
Antimicrobial activity comparison of different ZIF-8-based materials.

MOFs and MOFs based materials	Synthesis method	Targeted pathogens	Antimicrobial efficacy	Test value	Reference
ZIF-8@Rutin	C	*E. coli* *S. aureus*	Antibacterial activity due to Zn^{2+} ions release along with Rutin, with an even more important anti-inflammatory performance.	*n.i.*	[36]
Ag@ZIF-8	C	*E. coli* *S. aureus*	Bactericidal activity attributed to Zn and Ag ion release, which can bind to bacterial cell wall proteins, denaturing and deactivating them.	IZ = 29.5 mm IZ = 21 mm	[37]
Ag-X@ZIF-8	C	*E. coli* *S. aureus*	Ag-doped ZIF-8 significantly improves antibacterial activity compared to pure ZIF-8 by a combination of mechanisms such as membrane interaction, genetic interference and ROS generated.	IZ = 23 mm IZ = 25.2 mm	[38]
ZnO@ZIF-8	Schott	*E. coli* *S. aureus*	Antimicrobial action mainly due to the release of Zn^{2+} ions from ZnO nanorods, which disrupt bacterial cell membranes and interfere with cellular functions.	MBC = 0.25 mg/mL	[39]
Ag-Cu@ZIF-8@GO/PES	PI	*E. coli* *S. aureus*	Enhanced antibacterial activity through the release of Ag ions that disrupt the bacterial cells and copper further aiding by damaging cell walls.	IZ = 7.5 mm IZ = 0	[40]
Cu@ZIF-8/HA	HT	*E. coli*	Antibacterial effect attributed to controlled release of Cu^{2+} and Zn^{2+} ions. Copper ions disrupt bacterial membranes by interacting with SH- groups of proteins, altering permeability and leading to cell death. Zinc ions destabilize bacterial electrolyte balance and inhibit enzyme activity.	*n.i.*	[41]
Cu@ZIF-8 NWs	C	*E. coli*	Antibacterial mechanism involves controlled release of Cu^{2+} and Zn^{2+} ions, which disrupt bacterial cell membranes, generate oxidative stress via ROS and interfere with cellular metabolism.	MIC = 0.375 mg/mL	[42]
At10/CuS@ZIF-8	C	*E. coli* *S. aureus*	Bactericidal activity involves the irradiation with NIR light to bacterial disintegration, membrane rupture, and leakage of bacterial components.	MIC = 0.8 μmol/L	[43]
Ag-Cu@ZIF-8	CF-MC	*E. coli* *S. aureus* *C. albicans*	Enhanced antibacterial performance is achieved due to synergistic effect of Ag-Cu bimetallic system, most likely due to membrane disruption caused by Ag^{+} and Cu^{2+} ion release.	MIC = 0.1 mg/mL	*

C: conventional heating; PI: phase inversion; HT: hydrothermal; CF-MC: continuous-flow mechanochemistry; MIC: minimum inhibitory concentration; MBC: minimum bactericidal concentration; IZ: inhibitory zone; *n.i.*: not included; * This study.

Table 2
Textural properties of ZIF-8 and ZIF-8-based materials.

Sample	S_{BET} ($m^2\ g^{-1}$)	V_{BJH} ($cm^3\ g^{-1}$)	V_{MESO} ($cm^3\ g^{-1}$)	D_{BJH} (Å)
ZIF-8	1322	0.45	0.01	56
0.5 % Ag@ZIF-8	930	0.3	–	68
1 % Ag@ZIF-8	844	0.27	0.02	64
5 % Ag@ZIF-8	784	0.26	–	65
10 % Ag@ZIF-8	450	0.14	–	72
0.5 % Cu@ZIF-8	1345	0.45	0.02	56
1 % Cu@ZIF-8	1057	0.36	0.02	56
5 % Cu@ZIF-8	844	0.30	0.02	56
10 % Cu@ZIF-8	879	0.28	0.02	51

particularly zinc ions in the case of ZIF-8 [20]. Zinc ions exhibit potent antimicrobial properties by inducing cell deformation, causing rupture of the cell wall, leading to cytoplasm leakage, and creating an alkaline microenvironment. These effects collectively inhibit bacterial growth or result in bacterial death. Moreover, the ability to engineer ZIF-8 to control ion release adds to its appeal for various biomedical applications [21,22].

The antibacterial properties of ZIF-8 have found application in diverse fields, including implant coatings [23,24], water filtration [25,26], and multifunctional fabrics [27]. Understanding the chemistry of ZIF-8 particles and the kinetics of ion release in culture media is crucial for optimizing their antimicrobial efficiency [28]. Previous studies on the antibacterial effects of zinc oxide (ZnO) and silver nanoparticles (Ag NPs) highlighted variable cytotoxicity influenced by the interaction between the NPs and the constituents of the media [29–33]. Copper and its derivatives have garnered recognition as a notable metal renowned for its inherent antibacterial and antifungal properties, with instances wherein it supplants even silver due to its comparatively lower cost [34,35].

This study aligns with the growing interest in developing MOF-based materials with enhanced antimicrobial properties. The materials reported in the literature exhibit a variety of synthesis methods and mechanisms of action (Table 1).

For instance, studies performed by Xia et al. [36] and Thakur et al. [37] demonstrate that the release of metal ions (Zn^{2+} and Ag^{+}) plays a critical role in their antimicrobial activity, interacting with bacterial cell wall proteins and causing denaturation. Other materials, such as ZnO@ZIF-8, exhibit efficacy against a broader range of pathogens through membrane disruption mediated by Zn^{2+} ions [39]. Membrane disruption is also observed in Cu-based materials [41,42].

Hybrid materials Ag-Cu@ZIF-8 leverage the synergistic effects of bimetallic systems to enhance antimicrobial performance against bacteria and fungi, as explained by Makhetha et al. [40] and presented in this study, which shows minimum inhibitory concentration values of just 0.1 mg mL^{-1}. Positioning this material within the benchmark framework underscored its potential as an innovative solution to combat bacterial infections, contributing to the development of effective alternatives in the fight against antimicrobial resistance (Table 2).

2. Materials and methods

2.1. Materials

Reagents $Zn(NO_3)_2\ 6H_2O$, 2-methyl imidazole (99 %), $AgNO_3$, $Cu(NO_3)_2\ 2.5H_2O$, and methanol (99 %) were purchased from Sigma Aldrich and used without purification.

2.2. Synthesis of Ag@ZIF-8, Cu@ZIF-8, and Ag-Cu@ZIF-8

The synthesis of ZIF-8 was conducted in the prototype continuous flow mechanochemical DYNO®-MILL Research Lab reactor. To initiate the process, 0.01 mol of $Zn(NO_3)_2\ 6H_2O$ and 0.04 mol of 2-methyl imidazole (2-mIm) were combined with 100 mL of methanol. Under magnetic stirring, the reagents underwent dissolution over a period of approximately 10 min, after which the solution was introduced into the reactor through the feed hopper. The reaction chamber was filled to 55 % of its capacity with 1 mm diameter ZrO_2 microspheres. Synthesis transpired at room temperature for a total of 60 min, corresponding to a residence time of 33 min, with a grinding speed of 7.4 m s^{-1}. Post-reaction, the mixture was retrieved in a beaker, subjected to centrifugation for 10 min at 4000 rpm, and subsequently washed three times with methanol. Ultimately, the recovered solid was dried in an oven at 80 °C for 4 h to eliminate excess solvent from the structure.

Various concentrations of Ag were integrated into the framework of ZIF-8 utilizing a one-pot synthesis approach. This involves introducing Ag concentrations ranging from 0.5 to 10 % w/w into a reaction mixture comprising $Zn(NO_3)_2\ 6H_2O$ and 2-mIm. The reaction proceeded for a total duration of 60 min, resulting in a residence time of 33 min. Upon reaction completion, the resulting mixture was transferred into a beaker and subsequently subjected to centrifugation at 4000 rpm for 10 min.

For the synthesis of Cu@ZIF-8 materials, a similar protocol as described for Ag@ZIF-8 was followed. In this case, Cu concentrations ranging from 0.5 % to 10 % w/w, using $Cu(NO_3)_2\ 2.5H_2O$ as a reagent, were introduced into a reaction mixture containing $Zn(NO_3)_2\ 6H_2O$ and 2-mIm. The reaction proceeded over a total duration of 60 min (r.t. 33 min). Upon completion, the mixture was collected and transferred to a beaker, followed by centrifugation at 4000 rpm for 10 min to isolate the Cu@ZIF-8 material.

A similar one-pot approach was used to incorporate both Ag and Cu ions into the ZIF-8 framework to synthesize bimetallic Ag-Cu@ZIF-8. In this process, carefully measured amounts of Ag and Cu were added to a zinc-based precursor solution of $n(NO_3)_2\ 6H_2O$ and 2-mIm, enabling co-deposition of the metals within the ZIF-8 structure. The reaction proceeded under the same conditions as for Ag@ZIF-8 and Cu@ZIF-8, with a total reaction time of 60 min and a residence time of 33 min. After completion, the mixture was centrifuged at 4000 rpm for 10 min to isolate the Ag-Cu@ZIF-8 composite.

2.3. Characterization

X-ray diffraction (XRD) profiles of the samples were obtained in a Bruker D8 Advance diffractometer with a LynxEye detector. XRD patterns were recorded in a 2θ scan range from 4 to 70°. Bruker Diffractplus Eva software, supported by Powder Diffraction File database, was used for phase identification.

The chemical structure and the functional groups in the samples were evaluated by attenuated-total reflectance infrared spectroscopy (ATR-IR), performed by direct transmittance in a single-reflection (ATR top plate fixed to an optical beam condensing unit with ZnSe lens) with a MKII Golden Gate SPECAC instrument (Kent, UK). Spectra were recorded over 64 scans with a resolution of 4 cm^{-1} in a wavenumber range between 3500 and 400 cm^{-1}.

Brunauer–Emmett–Teller (BET) surface area and textural properties were analyzed by N_2 physisorption measurements (Micromeritics ASAP 2020 equipment). Samples were first degassed at 100 °C for 6 h and subsequently analyzed.

X-ray photoelectron spectroscopy (XPS) spectra were recorded on a Physical Electronic spectrometer (PHI Versa Probe II) using monochromatic Al Kαradiation (15 kV, 1486.6 eV), a dual beam charge neutralizer for analyzing the core-level signals of the elements of interest and a hemispherical multichannel detector. The sample spectra were recorded with a constant pass energy value of 29.35 eV, 0.125 eV/step and a beam diameter of 100 μm. XPS spectra were analyzed employing the XPS CASA software.

Transmission electron microscopy (TEM) images were acquired in a high-resolution transmission electron microscope Talos F200i (SCAI, UCO), equipped with a field emission gun (FEG) Schottky type with 200 kV operating voltage allowing to work in the range 20 to 200 kV, with STEM-HAADF transmission scanning imaging system.

2.4. Antimicrobial tests

An antibiogram was conducted to assess microbial susceptibility to each material developed in this work. The followed methodology was the Kirby-Bauer disk diffusion method (filter paper method) [44]. Briefly, fresh cultures of *E. coli, S. aureus*, and *C. albicans* were initially prepared as described above. Subsequently, a calibrated suspension of each microorganism was then prepared at a concentration of 1×10^6 CFU/mL, using Müller–Hinton broth (M-H, Sigma Aldrich) medium for bacterial species and Potato Dextrose Broth (PDB, Condalab, Spain) medium for yeast. 100 μL of each inoculum was spread onto Petri dishes (ø = 90 mm) containing M-H agar (Sigma Aldrich) or Potato Dextrose Agar (PDA, Condalab, Spain), respectively, through sterile Digralsky loops. Sterile filter paper disks were then placed onto each agar surface and impregnated with 50 μL of each material solution at the corresponding concentration. Positive controls consisted of filter paper disks soaked in $AgNO_3$ and $Cu(NO_3)_2$ solutions (5 % w/w), while negative controls were disks impregnated with MHB or PDB medium, depending on the microorganism. Finally, each Petri dish was incubated for 24 h at the optimal growth temperature for each microorganism. Following incubation, inhibition zone diameters (ϕ, mm) were measured using ImageJ software for Windows (National Institutes of Health, USA). These measurements enabled categorization of susceptibility according to CLSI standards, classifying each microorganism as susceptible (S, $\phi >$ 20 mm), intermediate (I, $15 < \phi < 19$ mm), or resistant (R, $\phi < 14$ mm) [45].

The Agricultural Chemistry, Soil Science and Microbiology Departments from University of Córdoba (Spain) provided the microbial strains employed in the experiments. These encompassed *Escherichia coli* CECT 102, NCIMB 9483 (from 'Colección Española de Cultivos Tipo', Universitat de València, Valencia, Spain), *Staphylococcus aureus* subsp. *Aureus* Rosenbach 1884 CECT 435 (from 'Colección Española de Cultivos Tipo', Universitat de València, Valencia, Spain), and *Candida albicans* SC5315, ATCC MYA-2876 (from the 'American Type Culture Collection', Manassas, Virginia, USA).

In parallel, both bactericidal and fungicidal activity of different concentrations of ZIF-8, Ag@ZIF-8, Cu@ZIF-8 and Ag-Cu@ZIF-8 (0.05, 0.1, 0.5, and 1 mg mL^{-1}) were evaluated using a 96-well plate antimicrobial susceptibility assay, a widely reported method in literature [46, 47]. For the assessment of microbial load reduction, bacterial strains were initially subcultured on Petri plates containing M-H agar at 37 °C for 24 h. Similarly, fresh fungal cultures were prepared on PDA at 28 °C for 24 h. Samples from these cultures were transferred to test tubes containing 10 mL of M-H broth. A spectrophotometer VR-2000, JP Selecta S.A. (Spain) was utilized to establish a specific initial microorganism quantity in each case. This was achieved by targeting an optical density of 0.08 to 0.13 at a wavelength of 625 nm, corresponding to, approximately, 1×10^8 CFU/mL for *E. coli* and *S. aureus*, and 1×10^6 CFU/mL for *C. albicans.* To standardize in all three cases the starting CFU per mL, bacterial cultures were diluted with M-H broth to 1×10^6 CFU/mL.

Regarding the experimental design, a 96-well plate was employed for each tested microorganism. In each well, 100 μL of standardized liquid culture and 100 μL of each MOF dilution in different concentrations were dispensed. Control groups included a 200 μL culture of M-H broth to demonstrate its sterility and 200 μL cultures of each microorganism without MOFs to assess the materials' impact on microbial growth. Three replicates were conducted for each test. Each plate was incubated for 24 h at the optimal growth temperature for the microorganisms. Following incubation, 50 μL from each well were cultured on M-H agar for bacterial strains and on PDA for yeast. Surface plating was performed using disposable plastic Digralsky loops, and the plates were incubated for 24 h to allow microbial growth. After incubation, colony-forming units (CFUs) were counted to evaluate the inhibitory potential of each synthesized material. The counting limit was set between 30 and 300 CFUs per plate. The experiment was conducted in triplicate, and the data presented represent the average of the triplicate results, with the standard deviation included. This method allowed a direct comparison of the antimicrobial activity of the synthesized materials against the control groups, providing a robust assessment of their efficacy in reducing microbial load.

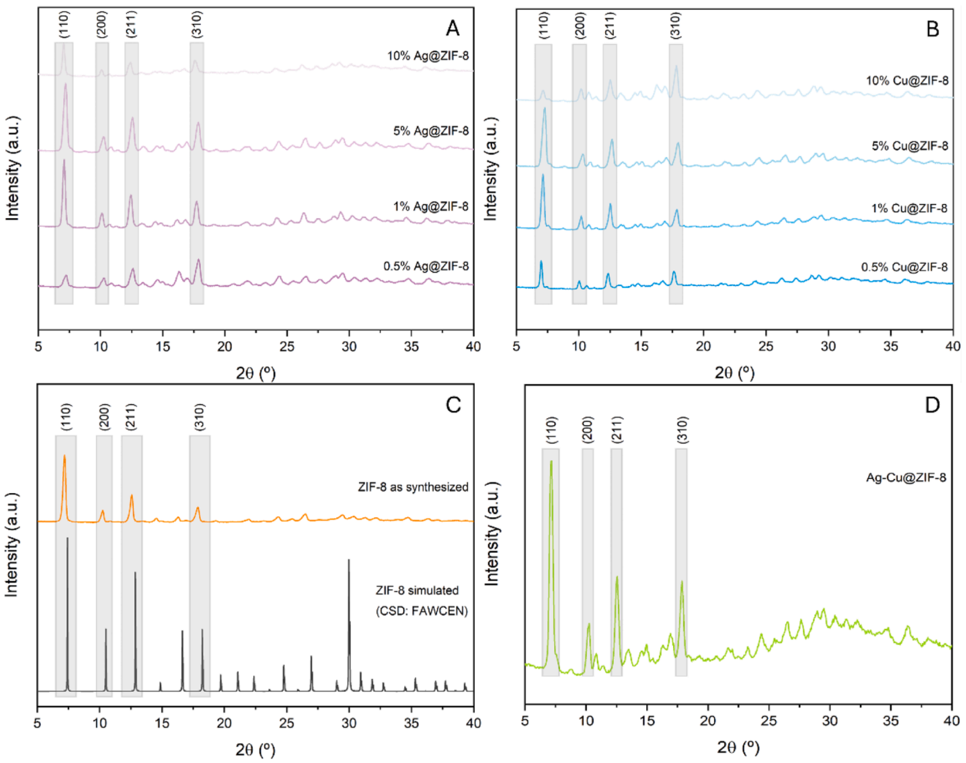

Fig. 1. XRD patterns of (A) Ag@ZIF-8, (B) Cu@ZIF-8. (C) simulated and as-synthesized ZIF-8, and (D) Ag-Cu@ZIF-8 materials.

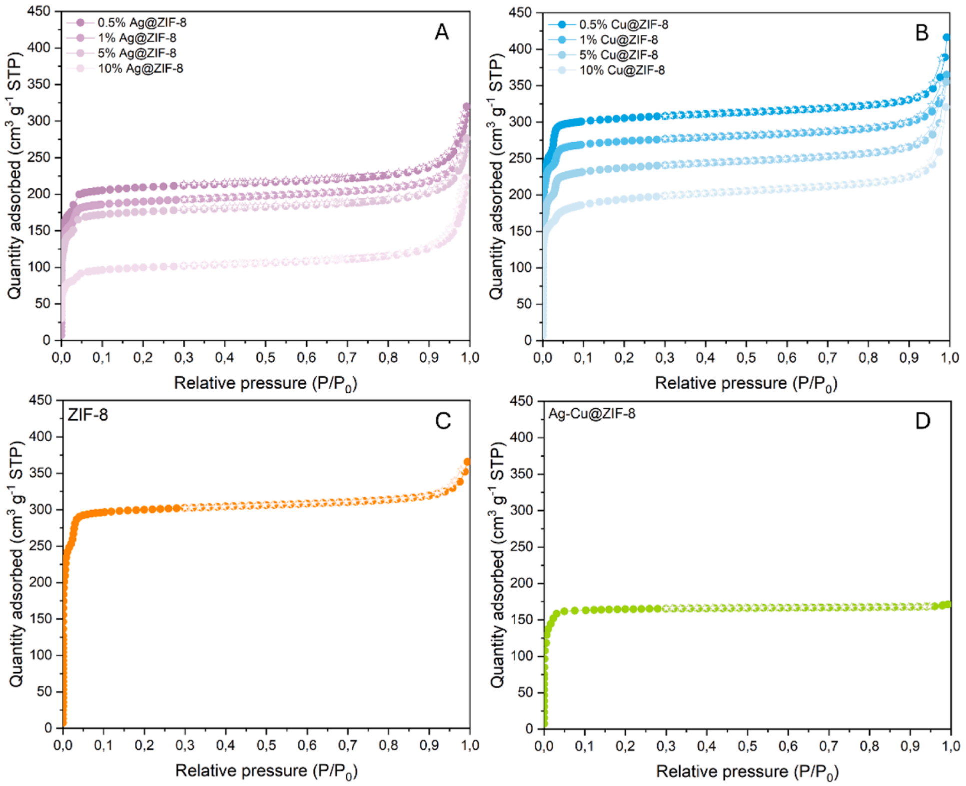

Fig. 2. BET N_2 adsorption/desorption isotherms at 77 K of (A) Ag@ZIF-8, (B) Cu@ZIF-8, (C) ZIF-8, and (D) Ag-Cu@ZIF-8 materials.

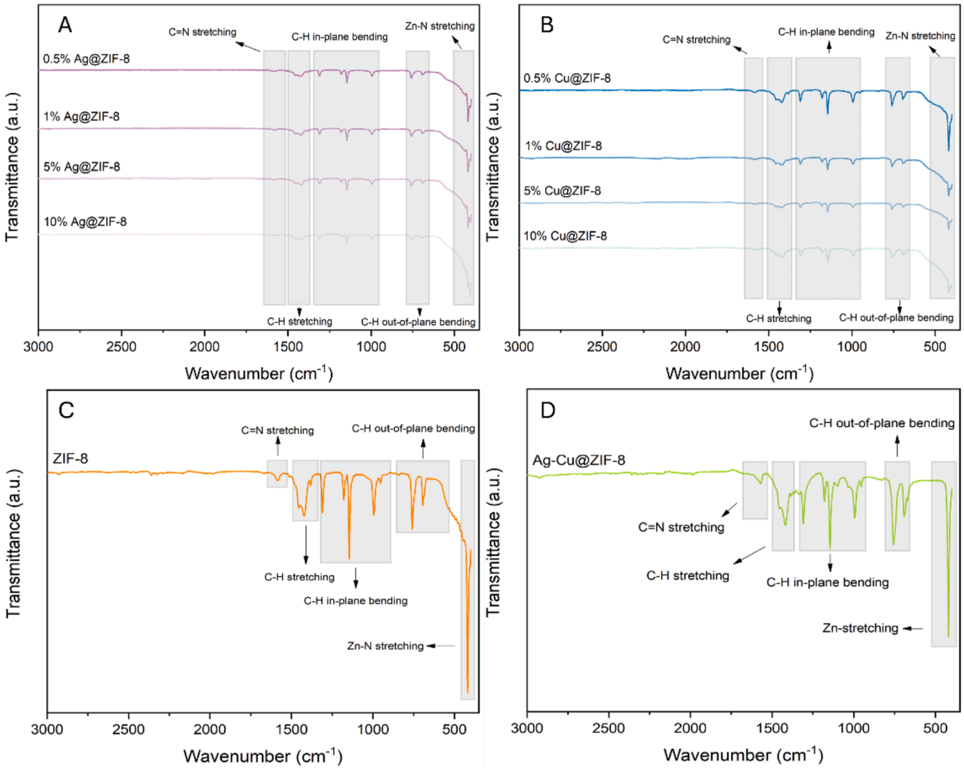

Fig. 3. ATR IR spectra of (A) Ag@ZIF-8, (B) Cu@ZIF-8, (C) ZIF-8, and (D) Ag-Cu@ZIF-8.

3. Results and discussion

3.1. *Characterization of the materials*

3.1.1. *XRD*

XRD analysis was conducted to confirm the structural integrity of the synthesized ZIF-8 and to assess any modifications in its crystallinity upon Ag and Cu incorporation. XRD patterns of the ZIF-8 framework (Fig. 1C) closely align with standard literature data, confirming that our synthesized ZIF-8 exhibits the expected sodalite-like crystalline structure. The characteristic peaks at 2θ values of 7.03°, 10.2°, 12.6°, and 17.7° correspond to (110), (200), (211), and (310) planes, respectively, which are typical of a high-quality ZIF-8 structure, in good agreement with previous reports [48–51].

For Ag@ZIF-8 (Fig. 1A), XRD patterns show the preservation of primary ZIF-8 peaks, indicating the incorporation of Ag did not significantly alter the framework's crystallinity or structural characteristics. This suggests the successful encapsulation of Ag nanoparticles without compromising the overall structure [52,53].

A slight shift in the 2θ values was comparatively observed in the case of Cu@ZIF-8 (Fig. 1B). This shift appears to increase with the concentration of Cu within the ZIF-8 matrix, implying a possible lattice distortion caused by the presence of Cu ions. This shift may be attributed to the ionic radius of Cu or potential interactions between Cu and the framework, subtly impacting the crystalline structure [54,55].

XRD patterns for the dual-metal-loaded Ag-Cu@ZIF-8 sample (Fig. 1D) continued to show alignment with standard ZIF-8 (as per Fig. 1C), albeit with slight modifications that reflect the combined presence of both Ag and Cu. The preservation of these peaks suggests that the sodalite-like framework of ZIF-8 remains unchanged, despite the introduction of multiple metal ions [40,56]. This resilience in structural integrity is essential, supporting the material's suitability for applications where both high crystallinity and metal incorporation are advantageous.

3.1.2. *BET analysis*

N_2 adsorption/desorption isotherms (Fig. 2) show a type-I profile, characteristic of microporous materials such as MOFs. This type of isotherm is marked by a sharp increase in nitrogen uptake at low relative pressures ($P/P_0 < 0.1$), which is indicative of a high concentration of micropores within the structure. The observed type-I behavior confirms the successful formation of a porous MOF framework with predominantly microporous characteristics, aligning with expectations for ZIF-8 and its metal-functionalized variants.

The high uptake at low pressures suggests a significant surface area and efficient micropore accessibility. This microporous nature, alongside the characteristic plateau at higher relative pressures, further supports the structural integrity and retention of ZIF-8 upon the incorporation of Ag and Cu. No significant hysteresis was observed, implying that the materials lack mesoporosity, which reinforces their classification as microporous structures. The stability of this microporous structure across all samples, even after metal incorporation, indicates minimum impact on pore accessibility, suggesting that the metal ions are likely well-dispersed within the framework without blocking the pore openings.

3.1.3. *IR analysis*

Fig. 3 shows ATR IR spectra of ZIF-8, Ag-doped, and Cu-modified samples, respectively. In all cases it is possible to detect the Zn—N stretching in the region of 400 cm^{-1}. This band is broader in the samples containing Ag and Cu due to the contribution of the incorporated metals in the structure. From 700 to 760 cm^{-1}, the out-of-plane bending bands of the imidazole ring are visible, decreasing in intensity in the modified materials. Additionally, the in-plane bending mode of the ring is present in the spectra from 950 to 1300 cm^{-1} and all samples exhibit the same behavior as mentioned for the out-of-plane mode. In the region from 1380 to 1450 cm^{-1}, the stretching vibrations from the C—H groups of the ring are clear as well as the characteristic stretching band corresponding to C═N (1580 cm^{-1}), decreasing in intensity at increasing metal loadings [57].

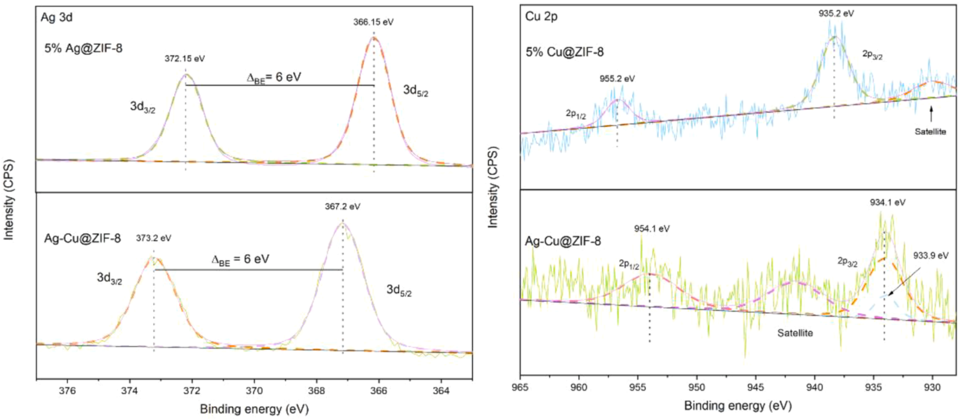

Fig. 4. High-resolution XPS spectra of Ag 3d orbital in 5 % Ag@ZIF-8 and Ag-Cu@ZIF-8, and Cu 2p region of 5 % Cu@ZIF-8 and Ag-Cu@ZIF-8 nanocomposite.

3.1.4. XPS

XPS high-resolution spectra of samples 5 % Ag@ZIF-8, 5 % Cu@ZIF-8, and Ag-Cu@ZIF-8 (Fig. 4) revealed significant insights into the electronic states of Ag and Cu within ZIF-8. In the Ag 3d region, a clear doublet can be observed, separated by approximately 6 eV, which is consistent with the expected spin-orbit of Ag 3d lines and suggests the presence of metallic Ag [40]. This spin-orbit, along with the precise binding energies, aligns with typical values for zero-valent Ag, indicating that Ag predominantly exists in a metallic state in Ag@ZIF-8 [58].

Interestingly, a notable shift to higher binding energy is observed for the Ag 3d peaks in Ag-Cu@ZIF-8 as compared to 5 % Ag@ZIF-8 sample. This shift could indicate a change in the local electronic environment around the Ag atoms, possibly due to interaction or alloying with Cu within the composite. Such a shift suggests that Ag atoms in Ag-Cu@ZIF-8 may be interacting with Cu atoms, which alters the electron density around Ag, resultsing in increased binding energy values. This observation hints a potential formation of an Ag-Cu composite phase, where electronic interactions between the two metals likely influence their individual oxidation states and binding energies [59].

The influence of this interaction is further supported by examining Cu 2p high-resolution spectra. In both Ag-Cu@ZIF-8 and 5 % Cu@ZIF-8, Cu 2p binding energies are consistent with those of reduced copper species and Cu (II) states, yet these peaks are shifted towards lower binding energy in Ag-Cu@ZIF-8 with respect to 5 % Cu@ZIF-8. This downward shift implies a reduction in the electron density around Cu, likely due to electron transfer between Cu and Ag. The observed shifts in both Ag and Cu spectra suggest a strong electronic coupling between Ag and Cu, possibly via electron transfer processes between copper species and Ag atoms, enhancing the stability and interaction within the ZIF-8 framework [60].

In both Cu-containing materials, the Cu 2p core level spectra exhibit distinct peaks for $2p_{1/2}$ and $2p_{3/2}$ levels, separated by approximately 20 eV. This separation is characteristic of Cu (II) oxidation states and aligns well with literature values for Cu 2p in CuO, confirming the presence of CuO in both 5 % Cu@ZIF-8 and Ag-Cu@ZIF-8 samples. This oxidation state suggests that, within the ZIF-8 framework, Cu predominantly exists as Cu (II), likely in the form of surface or dispersed CuO particles [61].

Ag-Cu@ZIF-8 exhibits a lower signal-to-noise ratio in the Cu 2p spectra, implying that Cu is present at a reduced concentration relative to 5 % Cu@ZIF-8. This lower concentration likely accounts for the increased noise and reduced peak intensity, as the signal strength in XPS is directly proportional to the concentration of the element. Such a reduced Cu concentration in Ag-Cu@ZIF-8 may result from competitive incorporation of Ag and Cu during synthesis, potentially favoring Ag over Cu or causing a less homogeneous distribution of Cu within the framework [59].

The presence of Cu (II) in both samples and the reduced Cu signal in Ag-Cu@ZIF-8 are notable, as these factors could influence some properties of the materials. Specifically, the partial incorporation of CuO could impact redox behavior, while the mixed-metal framework in Ag-Cu@ZIF-8 might influence the overall electron density and stability of both Ag and Cu sites, possibly enhancing synergistic effects between the metals.

3.1.5. TEM

Fig. 5 depicts TEM images of Ag@ZIF-8, Cu@ZIF-8 and Ag-Cu@ZIF-8, illustrating the distribution of metal nanoparticles on the ZIF-8 framework. Discrete Ag nanoparticles are clearly visible and well-dispersed across the surface for Ag@ZIF-8 and Ag-Cu@ZIF-8. This distribution suggests that Ag nanoparticles are effectively integrated into the framework, potentially contributing to enhanced surface activity and reactivity.

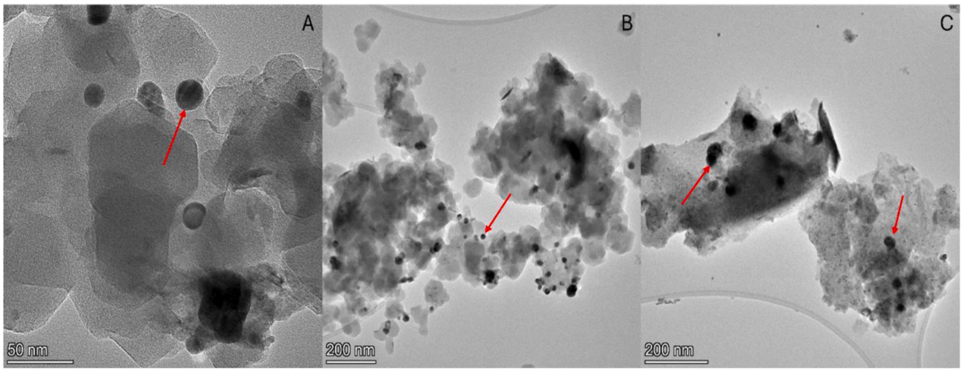

Fig. 5. TEM images of (A, B) Ag@ZIF-8 and (C), Ag-Cu@ZIF-8. Red arrows indicate the presence of Ag NPs with different shapes.

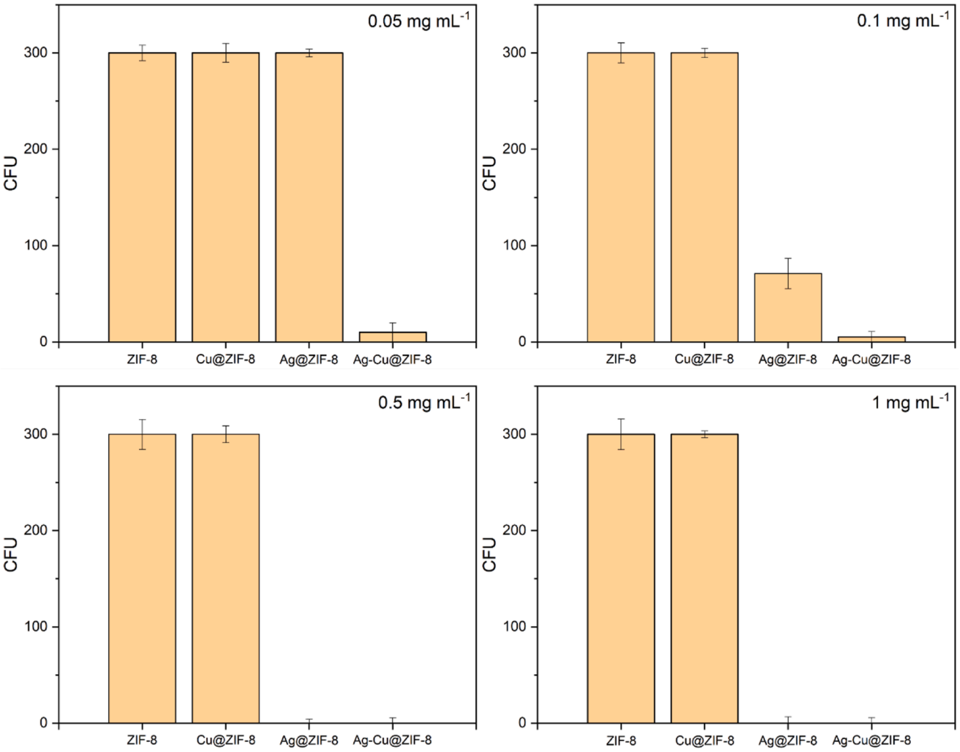

Fig. 6. Reduction of *E. coli* microbial load by different concentrations of ZIF-8, Cu@ZIF-8, Ag@ZIF-8 and Ag-Cu@ZIF-8.

In contrast, no distinct Cu nanoparticles are observed for Cu@ZIF-8 or Ag-Cu@ZIF-8. This lack of visible Cu particles may be due to several factors: (1) Cu nanoparticles might be extremely small, with sizes below the TEM resolution limit, resulting in a highly dispersed phase that prevents clear visualization, and (2) Cu has a lower atomic number than Ag, which leads to lower electron contrast in TEM images. Consequently, Cu nanoparticles may appear faint or remain undetectable against the ZIF-8 background, making them difficult to discern even if they are present on the materials surface.

The observations suggest that, while Ag forms visible nanoparticles on the ZIF-8 surface, Cu may be more finely distributed or even atomically dispersed within the framework, potentially influencing the materials electronic and catalytic properties differently from Ag. The high dispersion of Cu may facilitate unique catalytic interactions by increasing the available active sites, while Ag's more localized nanoparticle distribution might support specific plasmonic or redox behavior. The distinct dispersion characteristics of Ag and Cu in the Ag-Cu@ZIF-8 material could provide insights into the functional roles of each metal, particularly in applications where both localized and highly dispersed active sites are beneficial.

3.2. *Antimicrobial activity of the materials*

3.2.1. *Antibiograms results*

The antibiograms revealed that Ag-Cu@ZIF-8 demonstrated enhanced activity against *E. coli, S. aureus*, and *C. albicans* compared to monometallic variants and controls (Tables S1–and S3, respectively). At a concentration of 10 % w/w, Ag-Cu@ZIF-8 exhibited intermediate activity (I) against all tested microorganisms, with inhibition zones measuring 15.2 ± 1.0 mm, 15.8 ± 0.6 mm, and 18.1 ± 1.5 mm for *E. coli, S. aureus*, and *C. albicans*, respectively. In contrast, the monometallic materials showed limited or no activity, with microorganisms

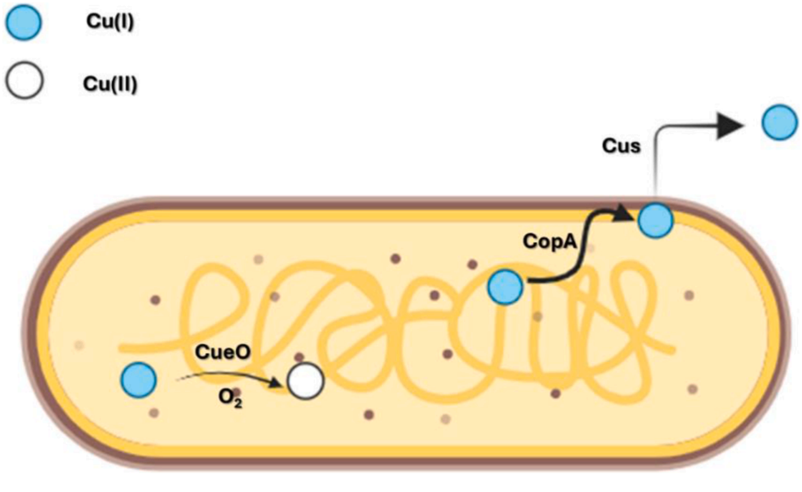

Fig. 7. Copper detoxification mechanisms for *E. coli.*

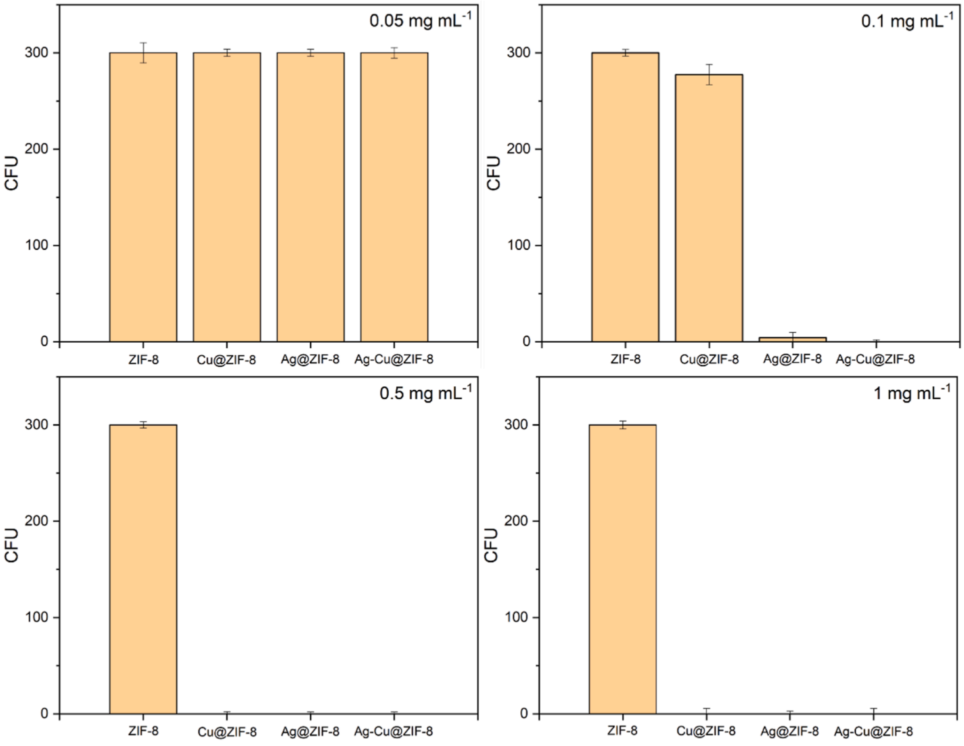

Fig. 8. Reduction of *S. aureus* microbial load by different concentrations of ZIF-8, Cu@ZIF-8, Ag@ZIF-8 and Ag-Cu@ZIF-8.

showing resistance (R) to these formulations.

The enhanced performance of the bimetallic system underscores the synergistic effects of the Ag-Cu composite, highlighting its potential as a promising candidate against multidrug-resistant pathogens.

3.2.2. *Antimicrobial activity against E. coli*

For Gram-negative bacteria, such as *E. coli*, the effect of Ag on the materials is significant (Fig. 6). Ag@ZIF-8 and the composite material Ag-Cu@ZIF-8 showed complete antibacterial activity using a small dose of 0.1 mg mL^{-1} as compared to virtually no activity recorded for ZIF-8 or Cu@ZIF-8. At the same time, almost no CFUs were observed when 0.05 mg mL^{-1} of the composite was employed, showing a synergistic effect between Ag NPs and copper species. This is in accordance with results observed in Table S1 (Fig. 7).

One explanation about the lack of inhibition from Cu ions could be since *E. coli* possesses some specific cellular resistance system against Cu toxicity. On the first hand, the P-type ATPase CopA facilitates the ATP-dependent transport of Cu (I) from the cytoplasm to the periplasm, while

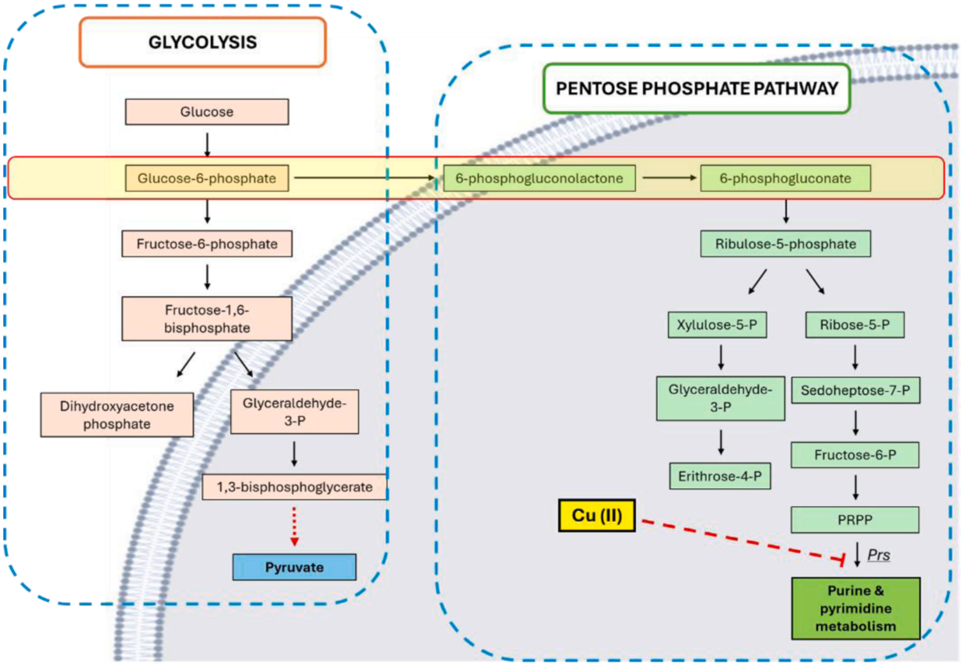

Fig. 9. Relationship between glycolysis and pentose phosphate pathway (PPP). Image adapted from reference [66].

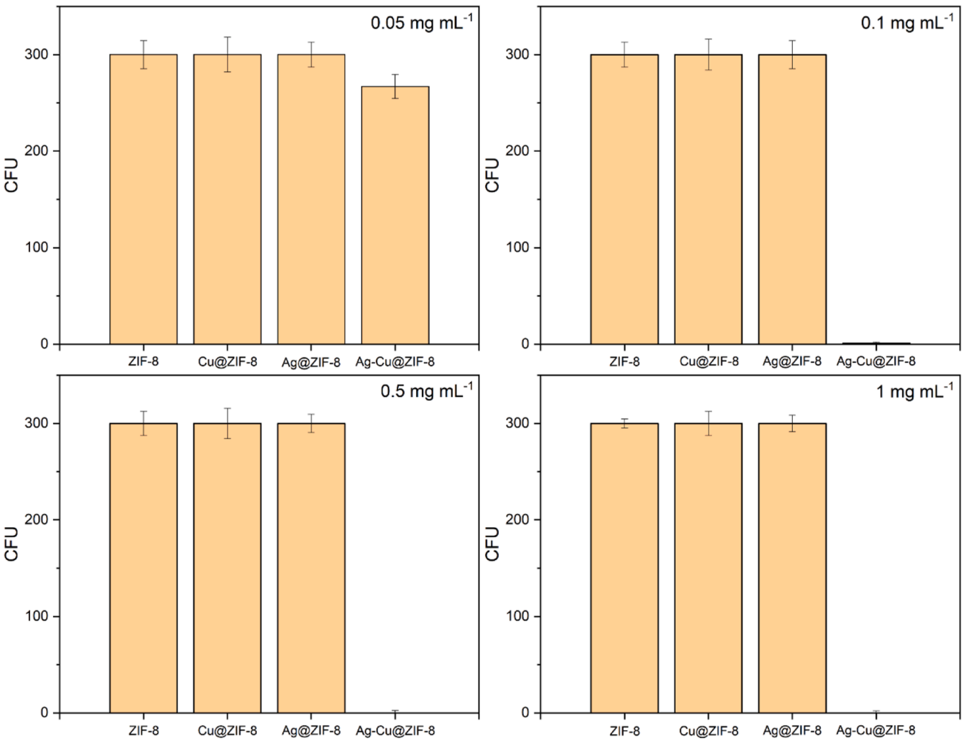

Fig. 10. Reduction of *C. albicans* microbial load by different concentrations of ZIF-8, Cu@ZIF-8, Ag@ZIF-8 and Ag-Cu@ZIF-8.

the Cus system mediates the exclusion of periplasmic Cu (I) from the cell. The elimination of periplasmic Cu (I) is facilitated by the copper chaperone CusF [62]. Additionally, the multicopper oxidase CueO plays a pivotal role in detoxification under aerobic conditions by oxidizing Cu (I) to Cu (II). Its enzymatic activity is contingent upon copper occupancy at all four multicopper oxidase Cu centers, alongside a fifth copper-binding site crucial for catalysis [63].

These mechanisms, along with structural features of Gram-negative bacteria, such as the outer membrane acting as a permeability barrier and the periplasm serving as a detoxification zone, confer higher resistance to Gram-positive bacteria for Cu. By compartmentalizing copper within the periplasm and employing specialized detoxification and export systems, Gram-negative bacteria maintain intracellular homeostasis and reduce copper-induced oxidative stress [64].

Remarkably, cells do not have any special mechanism against Ag incorporation into the cellular media. Unlike copper, microorganisms lack dedicated efflux pumps or transporters specifically tailored to expel silver ions from the cell [65].

3.2.3. Inhibition of *S. aureus* growth

Ag-Cu@ZIF-8 composite showed complete bactericidal activity at 0.1 mg mL^{-1} against *S. aureus*. Similarly, the monometallic material (Ag@ZIF-8) showed a significant decrease at the same concentration, with no visible colonies at 0.5 mg mL^{-1}. Remarkably, Cu@ZIF-8 could also inhibit the growth of the selected strain at 0.5 mg mL^{-1} (Fig. 8). These results are in good agreement with obtained antibiogram (Table S2).

In this case, the situation regarding antimicrobial resistance to copper differs from the trend for Gram-positive bacteria. It has been reported that Cu (II) perturbs carbon flux through the main metabolic pathways [66]. The Prs enzyme is the main target of Cu (II) in *S. aureus*. At the same time, this enzyme synthesized phosphoribosyl diphosphate (PPRP), a fundamental product of the pentose phosphate pathway [67], which occurs simultaneously to glycolysis (Fig. 9). Cu (II) exposure increases the concentration of metabolites implied in the synthesis of PRPP. By inhibiting the effect of Prs, the production of PRPP decreases, thus the rest of the products involved in the purine and pyrimidine metabolism, such as tryptophan, AMP, GMP, purines, pyrimidines, and nicotinamide dinucleotides [67,68].

Additionally, Cu (II) ions exhibit antimicrobial activity against *S. aureus* by inducing oxidative stress through the generation of reactive oxygen species, which damage lipids, proteins, and nucleic acids. This damage is enhanced by the inhibition of antioxidant enzymes such as catalase and glutathione. Furthermore, copper disrupts the integrity of the bacterial membrane, causing leakage of essential intracellular components, including proteins and sugars. It also interferes with the respiratory chain, impairing energy production and metabolic processes. While copper does not directly damage DNA integrity, it does inhibit the replication of critical genes, further reducing bacterial viability. These combined mechanisms highlight copper effectiveness in inhibiting *S. aureus* growth, making it a promising tool in combating bacterial infections [69].

3.2.4. Antifungal activity: inhibition of *C. albicans* growth

In the context of *C. albicans,* whereas Cu@ZIF-8 and Ag@ZIF-8, when considered individually, did not demonstrate inherent antifungal activity, the bimetallic system Ag-Cu@ZIF-8 manifested a notable reduction in the number of cells at 0.1 mg mL^{-1}, underscoring its efficacy in combating fungal growth (Fig. 10). These findings agree with those reported in Table S3.

One plausible explanation for this phenomenon lies in the unique composition of the fungal cell wall, characterized by abundant chitin and melanin polymers [70]. These constituents endow fungi with resilience against immune responses, antifungal treatments, and oxidative stress. The yeast-to-hyphal transition is a pivotal virulence mechanism that enables tissue invasion and robust biofilm formation [71]. This morphological shift, along with biofilm development, endows the fungus with significant resilience against immune defenses, antifungal treatments, and oxidative stress [72–74].

Biofilms consist of dense fungal communities embedded in an extracellular matrix, enhancing survival by acting as a physical and biochemical barrier. The application of the bimetallic Ag-Cu system has

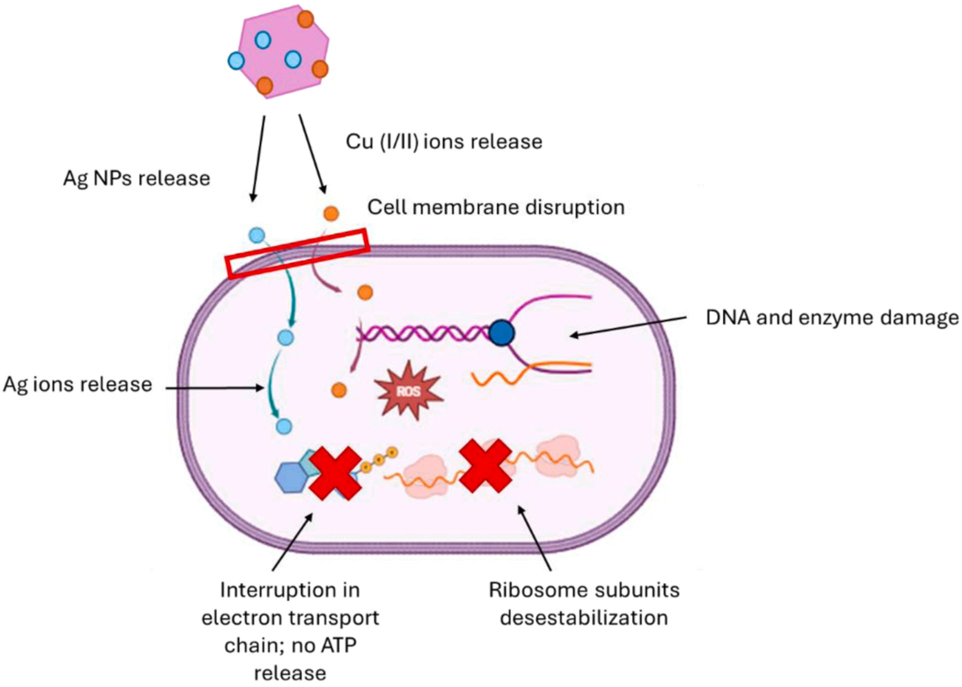

Fig. 11. Proposed mechanism of Ag-Cu@ZIF-8 against *C. albicans*.

demonstrated complete inhibition of these processes, suggesting interference with key cellular and molecular parameters. Specifically, the bimetallic system appears to target the yeast-to-hyphae transition by disrupting the pathways and signals that regulate morphological changes, thereby impairing the fungus' ability to invade tissues. Additionally, it significantly reduces biofilm formation by affecting cell adhesion, extracellular matrix production, and hydrolytic enzyme activity, which are crucial for biofilm and pathogenicity. This multifaceted disruption not only limits the structural development of biofilms but also compromises the expression of genes associated with fungal virulence, highlighting the potential of Ag-Cu systems as effective antifungal strategies [75–77]. Despite these investigations, further research is required to elucidate the precise mechanisms underlying the synergistic interaction between silver and copper in combating *C. albicans*. Understanding of this synergistic effect holds promise for the development of more effective antifungal strategies, addressing the persistent challenge of fungal infections (Fig. 11).

4. Conclusions

Ag- and Cu-modified ZIF-8-based systems were synthesized employing a novel beads-assisted flow process. This innovative approach aims to reduce time spent on synthesis while maintaining efficiency. The morphological and textural properties of the resulting materials pointed to the successful production of pure ZIF-8, along with the adequate incorporation of Ag nanoparticles and Cu into the system. The examination of the antimicrobial properties of these materials, against *E. coli, S. aureus*, and *C. albicans*, revealed a notable antimicrobial efficacy, with Ag-Cu@ZIF-8 bimetallic system exhibiting complete inhibition at an optimum level. Ag@ZIF-8 materials demonstrated excellent bactericidal activity (0.1 mg mL^{-1}) against *E. coli* and *S. aureus*. Cu@ZIF-8 showed a good antibacterial behavior against *S. aureus* (0.5 mg mL^{-1}, 5 % Cu loading), but no activity was noticed in *E. coli* or *C. albicans*. Noteworthy, when combining the same percentage in weight of Ag and Cu in the framework (5 % Ag + 5 % Cu), antifungal properties were exhibited as well with a 0.1 mg mL^{-1}, enhancing their antimicrobial properties due to a synergistic effect. This work establishes a starting point for continuous-flow beads-assisted protocols for synthesis of antimicrobial materials as well as the potential analysis on these nanomaterials in healthcare settings, such as safety testing with human cell lines and their effectiveness against other types of microorganisms including drug-resistant strains e.g. MRSA or *Pseudomonas aeruginosa*.

CRediT authorship contribution statement

Ana I. Martín-Perales: Writing – original draft, Methodology, Investigation, Formal analysis, Data curation, Conceptualization. **Manuel Peña-Ortiz:** Writing – original draft, Investigation, Formal analysis. **Juliana Alves Resende:** Writing – original draft, Visualization, Validation, Investigation, Formal analysis, Data curation. **Irene Malpartida:** Writing – original draft, Validation, Supervision, Resources, Project administration. **Rafael Luque:** Writing – review & editing, Validation, Supervision, Resources, Project administration, Funding acquisition, Conceptualization. **Alina M. Balu:** Writing – review & editing, Validation, Supervision, Resources, Project administration, Methodology, Funding acquisition.

Declaration of competing interest

The authors declare that they have no known competing financial interests or personal relationships that could have appeared to influence the work reported in this paper.

Acknowledgements

A.I. Martín-Perales acknowledges the company Deasyl S.A. for a research contract associated with this project. M. Peña-Ortiz gratefully acknowledges University of Córdoba for the financial support provided through the predoctoral contract "Contrato de Personal Investigador en Formación (PIF), submodalidad 2.2. del Plan Propio de Investigación 2021". Authors are highly grateful to Prof. Dr. José Ramos (Department of Microbiology, University of Córdoba), who is kindly acknowledged for his permission to utilize their facilities for various tests. The authors thank as well the Servicio Central de Apoyo a la Investigación (SCAI) from Universidad de Córdoba and Universidad de Málaga for the services in materials characterization. This publication was supported by RUDN University Strategic Academic Leadership Program (R. Luque).

Supplementary materials

Supplementary material associated with this article can be found, in the online version, at doi:10.1016/j.rineng.2024.103581.

Data availability

Data will be made available on request.

References

[1] C. Pettinari, R. Pettinari, C. Di Nicola, A. Tombesi, S. Scuri and F. Marchetti, *Coord. Chem. Rev.*, doi:10.1016/j.ccr.2021.214121.
[2] H.N. Abdelhamid, Curr. Med. Chem. 28 (2021) 7023–7075.
[3] D. Alezi, Y. Belmabkhout, M. Suyetin, P.M. Bhatt, L.J. Weseliński, V. Solovyeva, K. Adil, I. Spanopoulos, P.N. Trikalitis, A.H. Emwas, M. Eddaoudi, J. Am. Chem. Soc. 137 (2015) 13308–13318.
[4] S. Hiraide, Y. Sakanaka, H. Kajiro, S. Kawaguchi, M.T. Miyahara, H. Tanaka, Nat. Commun. 11 (2020) 4–17.
[5] M. Ronda-Leal, S.M. Osman, H.Won Jang, M. Shokouhimehr, A.A. Romero, R. Luque, Fuel 333 (2023) 126221.
[6] M. Liu, J. Wu, H. Hou, Chemistry 25 (2019) 2935–2948.
[7] M. Cai, L. Qin, L. You, Y. Yao, H. Wu, Z. Zhang, L. Zhang, X. Yin, J. Ni, RSC Adv. 10 (2020) 36862–36872.
[8] H.D. Lawson, S.P. Walton, C. Chan, ACS Appl. Mater. Interfaces 13 (2021) 7004–7020.
[9] H. Chai, K. Yu, Y. Zhao, Z. Zhang, S. Wang, C. Huang, X. Zhang, G. Zhang, Anal. Chem. 95 (2023) 10785–10794.
[10] C.Z. Wang, J. Chen, Q.H. Li, G.E. Wang, X.L. Ye, J. Lv and G. Xu, *Angew. Chem. - Int. Ed.*, doi:10.1002/anie.202302996.
[11] H.C. Zhou, J.R. Long, O.M. Yaghi, Chem. Rev. 112 (2012) 673–674.
[12] C.W. Jones, JACS Au 2 (2022) 1504–1505.
[13] M. Bergaoui, M. Khalfaoui, A. Awadallah-F, S. Al-Muhtaseb, J. Nat. Gas Sci. Eng. 96 (2021) 104289.
[14] D. Zou, D. Liu, J. Zhang, Energy Environ. Mater. 1 (2018) 209–220.
[15] S.S. Sankar, K. Karthick, K. Sangeetha, A. Karmakar, S. Kundu, ACS Omega 5 (2020) 57–67.
[16] Y.R. Lee, M.S. Jang, H.Y. Cho, H.J. Kwon, S. Kim, W.S. Ahn, Chem. Eng. J. 271 (2015) 276–280.
[17] K.S. Park, Z. Ni, A.P. Cote, J.Y. Choi, R. Huang, F.J. Uribe-Romo, H.K. Chae, M. O`Keeffe, O.M. Yaghi, Proc. Natl. Acad. Sci 103 (2006) 10186–10191.
[18] D. Fairen-Jimenez, S.A. Moggach, M.T. Wharmby, P.A. Wright, S. Parsons, T. Düren, J. Am. Chem. Soc. 133 (2011) 8900–8902.
[19] S.A. Moggach, T.D. Bennett, A.K. Cheetham, Angew. Chem. - Int. Ed. 48 (2009) 7087–7089.
[20] D. Ashok, M. Taheri, P. Garg, D. Webb, P. Parajuli, Y. Wang, B. Funnell, B. Taylor, D.C. Tscharke, T. Tsuzuki, N.K. Verma, A. Tricoli, D.R. Nisbet, Adv. Sci. 9 (2022) 1–15.
[21] J. Tan, D. Wang, H. Cao, Y. Qiao, H. Zhu, X. Liu, ACS Appl. Mater. Interfaces 10 (2018) 42018–42029.
[22] Y. Wang, A. Cao, Y. Jiang, X. Zhang, J. Liu, Y. Liu, ACS Appl. Mater. Interfaces 6 (2014) 2791–2798.
[23] M.A. Fardjahromi, F. Ejeian, A. Razmjou, G. Vesey, S.C. Mukhopadhyay, A. Derakhshan, M.E. Warkiani, Mater. Sci. Eng. C 123 (2021) 111972.
[24] K. Du, L. Su, X. Sun, X. Wang, Q. Wang, R. Li, B. Wang, Chem. Eng. J. (2024) 148576.
[25] V. Vatanpour, A. Yuksekdag, M. Ağtaş, M. Mehrabi, E. Salehi, R. Castro-Muñoz and I. Koyuncu, *Carbohydr. Polym.*, doi:10.1016/j.carbpol.2022.120230.
[26] R. Rodriguez, M.S. Palma, D. Bhandari, F. Tian, Langmuir 39 (2023) 2291–2300.
[27] H.S. Jhinjer, M. Jassal, A.K. Agrawal, Appl. Surf. Sci. 639 (2023) 158153.
[28] B.A. Costa, M.P. Abuçafy, T.W.L. Barbosa, B.L. da Silva, R.B. Fulindi, G. Isquibola, P.I. da Costa, L.A. Chiavacci, Pharmaceutics 15 (2023) 1–14.
[29] S. Agnihotri, S. Mukherji, S. Mukherji, RSC Adv. 4 (2014) 3974–3983.
[30] Z. Lu, K. Rong, J. Li, H. Yang, R. Chen, J. Mater. Sci. Mater. Med. 24 (2013) 1465–1471.
[31] P.M. Narayanan, W.S. Wilson, A.T. Abraham, M. Sevanan, Bionanoscience 2 (2012) 329–335.
[32] D.H. Jo, J.H. Kim, T.G. Lee, J.H. Kim, Nanomed. Nanotechnol., Biol. Med. 11 (2015) 1603–1611.
[33] R.C. De Souza, L.U. Haberbeck, H.G. Riella, D.H.B. Ribeiro, B.A.M. Carciofi, Braz. J. Chem. Eng. 36 (2019) 885–893.
[34] N. Jayarambabu, A. Akshaykranth, T. Venkatappa Rao, K. Venkateswara Rao, R. Rakesh Kumar, Mater. Lett. 259 (2020) 126813.
[35] S.P. Selvaraj, Mater. Today Proc 50 (2020) 2865–2868.
[36] X. Xia, X. Song, Y. Li, W. Hou, H. Lv, F. Li, Y. Li, J. Liu, X. Li, Front. Bioeng. Biotechnol. 10 (2022) 1–17.
[37] S. Thakur, S. Bharti, J. Environ. Nanotechnol. 13 (2024) 238–247.
[38] J. Abdi, Colloids Surf. A Physicochem. Eng. Asp. 604 (2020) 125330.
[39] J. Redfern, L. Geerts, J.W. Seo, J. Verran, L. Tosheva, L.H. Wee, ACS Appl. Nano Mater. 1 (2018) 1657–1665.
[40] T.A. Makhetha, R.M. Moutloali, J. Memb. Sci. 618 (2021) 118733.
[41] L. Ling, S. Cai, Y. Zuo, M. Tian, T. Meng, H. Tian, X. Bao, G. Xu, Colloids Surf. B Biointerfaces 219 (2022) 112810.
[42] A. Kumar, A. Sharma, Y. Chen, M.M. Jones, S.T. Vanyo, C. Li, M.B. Visser, S. D. Mahajan, R.K. Sharma, M.T. Swihart, Adv. Funct. Mater. 31 (2021) 1–13.
[43] D. Zhang, S. Bie, M. Anas Tomeh, X. Zhang, X. Zhao, Eur. J. Pharm. Biopharm. 204 (2024) 114516.
[44] J. Zhang, X. Yan, J. Liu, Y. Sun, Z. Guo, L. Wang, X. Wang, Z. Wang, L. Fan, J. Feng, S. Li, W. Yan, Sep. Purif. Technol. 287 (2022) 120619.
[45] *Methods for Dilution Antimicrobial Susceptibility Tests for Bacteria That Grow Aerobically ; Approved Standard — Ninth Edition*, 2012, vol. 32.
[46] J. Redfern, L. Geerts, J.W. Seo, J. Verran, L. Tosheva and L.H. Wee, *Eur. Respir. J.*, doi:10.1183/13993003.00239-2022.
[47] M. Müsken, S. Di Fiore, U. Römling, S. Häussler, Nat. Protoc. 5 (2010) 1460–1469.
[48] X. Guo, S. He, Z. Meng, Y. Wang, Y. Peng, RSC Adv. 12 (2022) 17919–17931.
[49] G.A. Cobian-Solorio, I.A. Aguayo-Villarreal, C.K. Rojas-Mayorga, R. Muñiz-Valencia, M.J. Emparan-Legaspi and N.E. Davila Guzman, *J. Mol. Struct.*, doi:10.1016/j.molstruc.2024.139698.
[50] D. Refaat, M. Yahia, J. Coronas, Process Saf. Environ. Prot. 192 (2024) 401–411.
[51] C.A. Castilla-Martinez, C. Charmette, J. Cartier, U.B. Demirci, New J. Chem. 48 (2024) 8534–8544.
[52] Q. Bin, M. Wang and L. Wang, *Nanotechnology*, doi:10.1088/1361-6528/ab5cde.
[53] J. Xiao, S. Zhu, L. Bu, Y. Chen, R. Wu, S. Zhou, RSC Adv. 13 (2023) 27203–27211.
[54] A. Awadallah-F, F. Hillman, S.A. Al-Muhtaseb, H.K. Jeong, J. Mater. Sci. 54 (2019) 5513–5527.
[55] B. Qi, X. Wang, X. Wang, J. Cheng, Y. Shang, Nanomaterials 12 (2022) 1–11.
[56] J. Zhang, X. Xie, X. He, X. Gong, X. Zhang, A. Liu and Y. Huang, *J. Alloys Compd.*, doi:10.1016/j.jallcom.2023.172802.
[57] F. Cacho-Bailo, B. Seoane, C. Téllez, J. Coronas, J. Memb. Sci. 464 (2014) 119–126.
[58] S. Gan, M. Qiu, L. Li, Y. Li, D. Su, Z. Jia, Y. Xia, W. Xu, D. Yang, J. Lei and J. Liu, *Ind. Crops Prod.*, doi:10.1016/j.indcrop.2023.117803.
[59] J.R. Deka, D. Saikia, T.H. Cheng, H.M. Kao, Y.C. Yang, J. Environ. Chem. Eng. 11 (2023) 109777.
[60] Z. Yang, C. Ma, W. Wang, M. Zhang, X. Hao, S. Chen, J. Colloid Interface Sci. 557 (2019) 156–167.
[61] S. Kaja, A. Nag, Langmuir 37 (2021) 13027–13037.
[62] C. Petersen, L.B. Møller, Gene 261 (2000) 289–298.
[63] C. Rensing, G. Grass, FEMS Microbiol. Rev. 27 (2003) 197–213.
[64] J. ichi Ishihara, T. Mekubo, C. Kusaka, S. Kondo, R. Oiko, K. Igarashi, H. Aiba, S. Ishikawa, N. Ogasawara, T. Oshima, H. Takahashi, Biosystems 231 (2023) 104980.
[65] E.O. Mikhailova, *J. Funct. Biomater.*, doi:10.3390/jfb11040084.
[66] E. Tarrant, G. Riboldi, M.R. McIlvin, J. Stevenson, A. Barwinska-Sendra, L. J. Stewart, M.A. Saito, K.J. Waldron, Metallomics 11 (2019) 183–200.
[67] J. Norambuena, H. Al-Tameemi, H. Bovermann, J. Kim, W.N. Beavers, E.P. Skaar, D. Parker, J.M. Boyd, PLoS. Pathog. 19 (2023) 1–28.
[68] E.E. Price, J.M. Boyd, Trends. Microbiol. 28 (2020) 821–831.
[69] M. Li, Z. Ma, Y. Zhu, H. Xia, M. Yao, X. Chu, X. Wang, K. Yang, M. Yang, Y. Zhang, C. Mao, Adv. Healthc. Mater. 5 (2016) 557–566.
[70] R. Garcia-Rubio, H.C. de Oliveira, J. Rivera, N. Trevijano-Contador, Front. Microbiol. 10 (2020) 1–13.
[71] T. Vila, J.A. Romo, C.G. Pierce, S.F. McHardy, S.P. Saville, J.L. Lopez-Ribot, Virulence 8 (2017) 150–158.
[72] H. Jing, Z. Yu, L. Li, J. Biomed. Mater. Res. - Part A 87 (2008) 33–37.
[73] M.R. Kamli, M.A. Malik, S.A. Lone, J.S.M. Sabir, E.H. Mattar, A. Ahmad, Pharmaceutics 13 (2021) 1957.
[74] M. Paszkiewicz, A. Gołąbiewska, Ł. Rajski, E. Kowal, A. Sajdak, A. Zaleska-Medynska, J. Nanomater. 2016 (2016) 1–11.
[75] S. Muthamil, V.A. Devi, B. Balasubramaniam, K. Balamurugan, S.K. Pandian, J. Basic Microbiol. 58 (2018) 343–357.
[76] F. Martinez-Gutierrez, L. Boegli, A. Agostinho, E.M. Sánchez, H. Bach, F. Ruiz, G. James, Biofouling 29 (2013) 651–660.
[77] G. Rahimi, A. Khodavandi and R. Yaghobi, *Micro Nano Biomed.*, doi:10.15412/j.mnb.05010102.